JET–R(99)05

T Loarer et al

D_α Measurements in the JET Divertor with the Divertor Periscope Diagnostic

JET–R(99)05

D_α Measurements in the JET Divertor with the Divertor Periscope Diagnostic

T Loarer[1], L D Horton, H Kubo[2], C F Maggi, P D Morgan, M F Stamp, M von Hellermann.

JET Joint Undertaking, Abingdon, Oxfordshire, OX14 3EA,
[1]CEA Cadarache, F-13108 St Paul-lez-Durance, France.
[2]Naka Fusion Research Establishment, JAERI, 311-01 Japan.

September 1999

1. INTRODUCTION

The understanding of plasma surface interactions, in order to assess the main processes which take place in the divertor region, requires knowledge of the plasma characteristics. In JET, the characterisation of the different divertor geometry for the successive Mark I, Mark IIA, Mark IIAP (the "plugged" version of Mark IIA) and finally Mark IIGB divertors entails knowledge of plasma parameters such as ion and electron density, n_i and n_e, ion and electron temperature, T_i and T_e, and the recycling particle flux at the edge. Whereas the particle recycling can be estimated by measuring the intensity of D_α line emission, neither n_i nor T_i can be easily and routinely obtained, compared to n_e and T_e, which are measured by Langmuir probes.

In JET, two periscopes have been installed in the divertor region [1]. The periscope installed outboard of the divertor has lines-of-sight which traverse the divertor plasma and terminate on recycling surfaces covering the inner half of the divertor. The optical system installed in this outer periscope consists of 10 optical fibres which transfer light to a high resolution spectrometer. Typically, lines such as D_α, CII (λ = 6578 Å) and CIII (λ = 4650 Å) have been measured. With this spectrometer, it is possible to measure the D_α line profile shape and thus the energy distribution of the emitting neutrals. The ion temperature can then be deduced under some assumptions. A previous analysis by Kubo [2] has shown that, even if there were some key questions concerning the alignment of the optical viewing lines, the D^+ ion temperature could be estimated from the fitting of the D_α spectrum.

The first part of this report concentrates on the measurement of D_α line emission, its fitting and the plasma parameters which can be deduced from the spectrum fitting. The second section is devoted to the description of the spectrometer. Using spatial profiles of the ion saturation current measured by Langmuir probes and of the D_α and CII emission measured by the periscope, the geometry of the viewing chords was checked. The geometry proposed here results in better agreement between the experimental measurements and modelling. The D_α emission measured by the different channels is then discussed in section 3 for Ohmic and L-mode density limit discharges. It is shown that the D_α signals which intersect the divertor target in the private region and in the main SOL behave in an opposite way as detachment occurs. Using these different evolutions, a degree of detachment (DoD) based on the D_α emission of two adjacent channels is defined, complementary to the DoD [3] derived from the ion saturation current measured by the target Langmuir probes. The radius of the maximum emission of D_α is discussed in section 4. The resulting energy of the atoms (fast and slow) is also presented in this section. In section 5, the measured D_α spectra are compared to initial simulated spectra based on two dimensional edge plasma/neutral modelling. In the last section conclusions are drawn and possible future improvements are outlined.

2. ENERGY DISTRIBUTION OF THE DEUTERIUM NEUTRALS AND THE D_α LINE PROFILE

The spectral profile of the D_α line emitted from the divertor plasma region contains information on the energy distribution of the deuterium atoms and their recycling processes. Impacting ions and atoms on the tiles of the divertor can be either reflected as D neutrals or absorbed by the wall. The reflected atoms can either be ionised or experience a charge exchange collision. Their energy (before any charge exchange collisions) is of the order of the impacting particle, i.e. about 2 times [4] the initial energy of the ion (~10 eV for JET divertor plasma conditions) before sheath acceleration.

When the wall becomes saturated, the absorbed atoms are released as D_2 molecules with an energy of the surface temperature of the wall (in JET, 300-600 K ~ 0.02-0.05 eV). The wall becomes therefore a D_2 source which balances the rate of absorbtion of atoms and ions. These molecules experience dissociation or ionisation by collision with the electrons producing D_2^+, D_o or D^+. In the vicinity of the divertor target ($n_e \sim 10^{19}$ m^{-3} and $T_e \leq 10$ eV), the D_2 molecules and D_2^+ molecular ions are essentially instantaneously dissociated (mean free path ~ 1cm) and the resulting deuterium atoms move at the velocity determined by their Franck-Condon (FC) energy (3-4 eV) until they experience a charge exchange reaction, are ionised by electron collision or return to the divertor tile. In the case of charge exchange, the neutralised atom acquires the ion energy.

The energy distribution of the deuterium atoms is therefore composed of a low energy component (“slow” atoms, resulting from molecular dissociation and ionisation) and a high energy component (“fast” atoms, resulting from the reflected atoms and atoms produced by charge exchange collisions).

In general, the spectrum of D_α emission from such a neutral energy distribution is further complicated by the Zeeman effect. In JET divertor plasma conditions, the Zeeman splitting is typically greater than Doppler broadening of the slow component of the emission and comparable to the broadening of the fast component. Since the magnitude of the Zeeman splitting depends on the magnetic field strength at the point of emission, it provides information on the spatial location of the emission along the line of sight.

Finally, the D_α spectrum in JET can consist of a superposition of emission of any of the three isotopes of hydrogen. The three spectra are slightly shifted with respect to each other and must be fitted separately. Information on the isotopic content of the recycling neutrals is therefore available and has been used to great effect in JET DT experiments [5]. In the spectra considered here, the dominant isotope is deuterium; there is essentially no tritium and the hydrogen emission is less than 1.5% of the deuterium emission.

Figure 1 shows a typical D_α line profile observed in the JET divertor with a visible spectrometer whose line of sight views the divertor from the top of the machine. The spectrometer

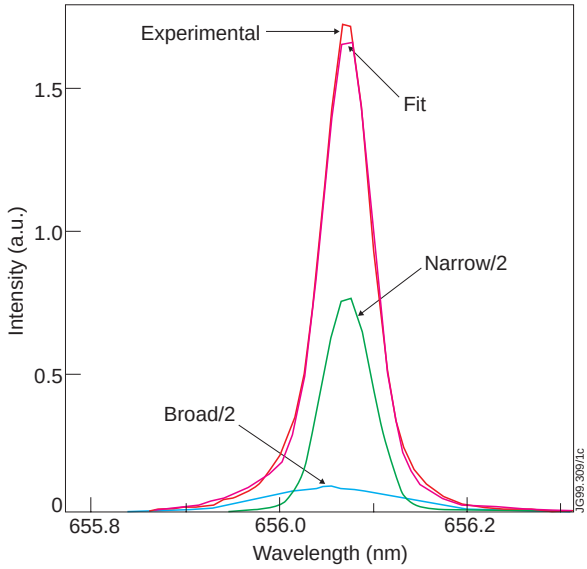

Figure 1: Line profile of D_α emission from the JET divertor. The diagnostic views the divertor from the top of the machine and is equipped with a polarizer which passes only the linearly polarized component of the light. The fitted profile is the sum of two gaussian components, shown here at half intensity.

is equipped with a linear polarizer so that only the Zeeman π component is observed. The fitted profile is the sum of two gaussions, fitting a narrow and a broad component, as shown in figure 1. The narrow component corresponds to emission of the excited slow atoms after dissociative electron impact excitation and of Franck-Condon D atoms (originating both from the wall and from external D_2 gas injection into the divertor). The broad component is due to the emission of charge exchange neutrals and of fast neutrals reflected by the wall following neutral or ion impact.

The D_α profile is also modified by the Doppler shift of the spectrum toward the lower wavelength for the fast reflected atoms. This is due to the fact that the reflected atoms move away from the divertor tile and most of them move toward the spectrometer. This shift is expressed as $\Delta\lambda=(v/c)\lambda_o$, where v is the velocity component of the excited atom in the direction of observation, c is the velocity of light and λ_o is the wavelength of emission by a particle at rest.

Since the energies of the reflected and charge exchange atoms are very similar, it becomes difficult to distinguish these two contributions to the broad component. However, it can be seen in figure 1 that the fit is in good agreement with the measured spectrum, the Doppler shift being taken into account by a shift of the broad component towards lower wavelength.

It is not always possible to equip the collection system with a polarizer and, as a consequence, both the narrow and the broad components are strongly influenced by the Zeeman effect produced by the confining magnetic field. This is shown in the spectrum of figure 2, obtained with the divertor periscope, where the three Zeeman components, σ^-, π and σ^+, of the narrow component of the D_α spectrum can be

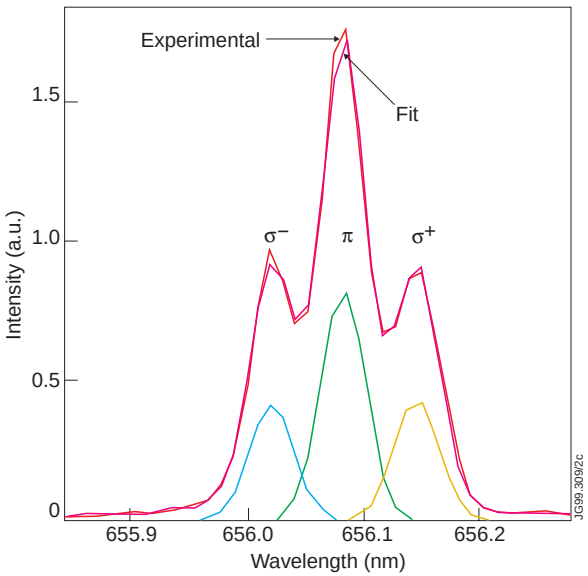

Figure 2: Experimental and fitted D_α spectrum as a function of wavelength for D_α detection without polarizer. The three Zeeman components σ-, π and σ+ are clearly distinguishable for the narrow component (shown individually at half amplitude). The broad component is also fit with 3 gaussians (not shown) whose amplitudes are low.

clearly distinguished. The splitting of the two sigma components from the central π component is given by

$$\pm\Delta E = \hbar(\pm\Delta\omega) = \mu_B B \tag{1}$$

where $\pm\Delta E$ ($\pm\Delta\omega$) is the energy (angular frequency) shift of the $\sigma^{+/-}$ component relative to the π component of the emission and $\mu_B = e\hbar/2m_e$ is the Bohr magneton. This shift is converted into wavelength as follows:

$$(\lambda_0 + \Delta\lambda) = \frac{2\pi c}{\omega_0 + \Delta\omega}. \tag{2}$$

Assuming that the frequency shift is small compared to the unperturbed frequency, one obtains:

$$\Delta\lambda \approx \lambda_0^2 \frac{\Delta\omega}{2\pi c} \tag{3}$$

or

$$\Delta\lambda\,[\text{Å}] \approx 4.67\times10^{-9}\lambda_0^2\,[\text{Å}]\,B\,[\text{T}]. \tag{4}$$

For the D_α transition, one obtains a Zeeman splitting of ±0.201 Å per Tesla.

The effect of Zeeman splitting is not easily seen in the broad component, due to its weak intensity and the fact that its Doppler width is comparable to the splitting. Nevertheless, the D_α spectrum is well reproduced with the sum of 6 gaussians which fit the σ^-, π and σ^+ peaks of both the narrow and broad component. The details of the fitting algorithm and how it was employed are described in Appendix A. The program used is an old routine originally intended to fit H and D Zeeman-split spectra and currently is somewhat restrictive for the purpose it is applied here. In particular, the program does not allow for a time-dependent Zeeman splitting for the warm components.

One can exploit the Zeeman effect to deduce the local magnetic field at the point of emission from the wavelength difference between the $\sigma^{-/+}$ and the π components. Knowing the variation of the total magnetic field with major radius ($B = B_0(R_0/R)$ where B_o is the magnetic field at the R_o radius), one can determine an average position of D_α emission along each line of sight. Since the position of the cold components can be accurately determined (typically ±0.03-0.04 pixels), the position of emission can be determined to an accuracy of about 1%.

3. THE DIVERTOR PERISCOPE DIAGNOSTIC

The divertor periscope diagnostic (KT6A) is composed of a high resolution spectrometer connected to a periscope [1] viewing the inner divertor from the outer side. Figure 3 shows a schematic view of the 10 lines of sight of the periscope. A second periscope, not shown on the figure, viewing the outer target plates of the divertor from the inner side can also be connected to this

spectrometer. However, in the following we will report measurements only from the outer periscope viewing the inner divertor. The spot diameter of each line of sight at the inner divertor target is about 25 mm, while the distance between each channel is about 55 mm. The wavelength range covered for a given grating position is 8 nm with a dispersion of 0.011 nm per pixel, corresponding to a wavelength resolution of 0.027 nm and to an equivalent energy resolution of 0.57 eV for D^o. The time resolution is 100 ms.

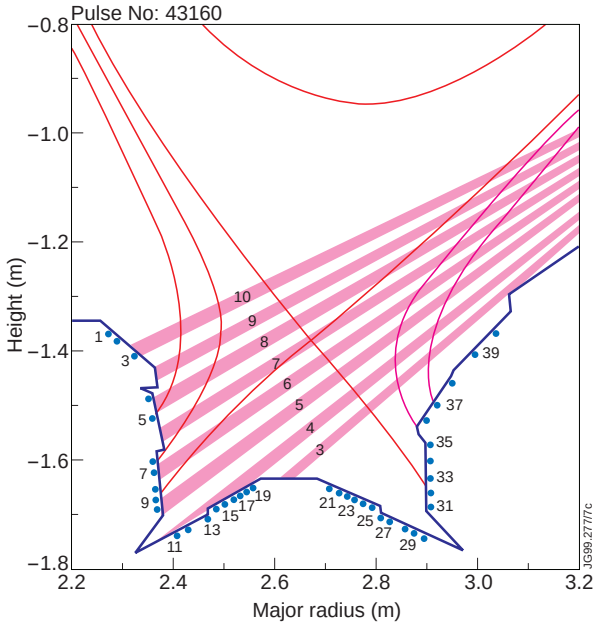

Figure 3: View of the high resolution spectrometer KT6A with its 10 tracks. Tracks 1, 2 (not shown) and 3 are completely vignetted by the divertor structure. Also shown are the positions of the fixed Langmuir probes which are mounted in the divertor targets.

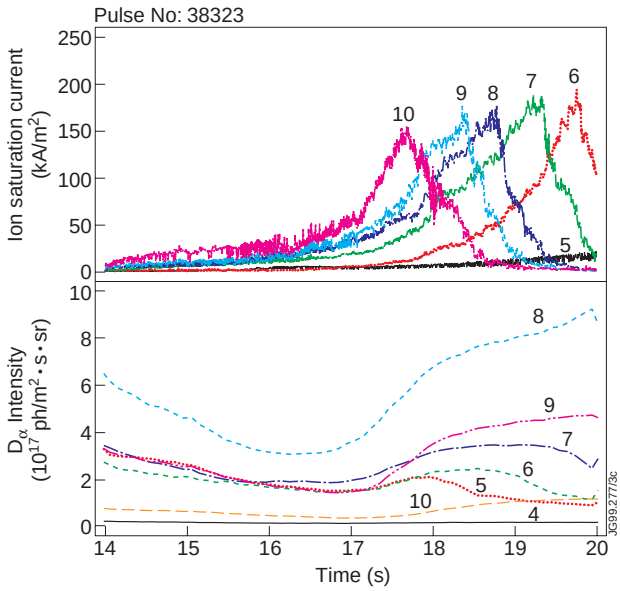

Figure 4: Time evolution for a probe calibration pulse of ion saturation current from the Langmuir probes located on the inner vertical target (Probes 5 to 10 - top panel) and the D_α signals from tracks 4 to 10 of KT6A (bottom panel).

Previous work on the data obtained with this diagnostic highlighted that there was a problem with the reference geometry of the lines of sight [2]. The geometry has been checked using pulses designed for the calibration of the divertor Langmuir probes, where the strike points are moved from the horizontal to the vertical target at about constant plasma density. In figure 4 are plotted the time evolution of the D_α signals measured by tracks 4-10 of KT6A and the ion saturation current (J_{sat}) measured with Langmuir probes 5 to 10 for a typical probe calibration shot. Tracks 1-3 of KT6A are found to have little or no signal and are thus deduced to be blocked by the tiles of the outer divertor. The maximum of the saturation current obtained on each probe occurs at a time when the inner strike point is very close (within a few mm) to that probe. Both CII emission (λ=6578 Å) and D_α have been used in order to determine the geometry of the KT6A lines of sight. For $n_e = 3\times10^{19}$ m^{-3} and $T_e = 10$ eV, which are values typical of the divertor plasma in these pulses, and assuming the emitting ions / atoms move with a thermal velocity of 10^3 m/s, the mean free path of ionisation, λ_i, of C^+ and D^0 are calculated to be about

1 and 3 cm respectively. As a consequence, the maximum emission of both CII and D_α is estimated to be close to the strike point.

In order for tracks 1 to 3 to be vignetted by the divertor structure, track 4 must be nearly tangent to the bottom inner divertor tiles. Such a geometry means that the signal from channel 4 will be integrated over a rather wide major radius range: typically from R=2.35 to 2.60 m. This is confirmed by the fact that the signal from track 4 does not exhibit as large an amplitude variation as those from tracks 5 to 8 when the strike point is moved across the target. By cross-checking the time evolution of D_α, CII and J_{sat}, it has been possible to define the geometry displayed in figure 3. It should be noted that this geometry is close to the one which has been deduced from in-vessel measurements of the position of the lines of sight at atmospheric pressure and at room temperature (~20°C). The difference between the two geometries corresponds to an anticlockwise rotation of 2° of the line of sight and is probably linked to deformations of the vessel from both the vacuum and thermal forces (the temperature of the vessel when operating is ~320°C). Probe calibration shots are performed regularly in order to estimate probe tip erosion and it appears that the KT6A alignment does not change significantly with time as no change has been observed between the Mark IIA and the Mark IIAP divertor campaigns. The geometry proposed here is consistent with vignetting of channels 1 to 3.

4. OHMIC AND L-MODE DENSITY LIMIT PULSES

During the Mark IIA campaign, a series of experiments in Ohmic and L-mode plasmas (I_p=2 MA, B_T=2.5 T) has been performed in deuterium (isotopic ratio $n_H/(n_H+n_D)<5\%$) in order to study the density limit and plasma detachment [6]. Figure 5 shows the time evolution of the main plasma parameters for one of these discharges with vertical target configuration: volume averaged plasma density $<n_e>$, total input power (P_{in}), radiated power (P_{rad}) and ion saturation current (J_{sat}) measured by a Langmuir probe (probe 7, see figure 3) located on the inner target in the SOL and close to the inner strike point. A nearly linear $<n_e>$ increase from 2×10^{19} m^{-3} to 2.7×10^{19} m^{-3} is recorded while the radiation fraction $\gamma = P_{rad}/P_{tot}$ increases from ~50 to 60%. With increasing gas fuelling, J_{sat} increases and then starts to decrease. At ~19.4 s (the time marked 'M' in

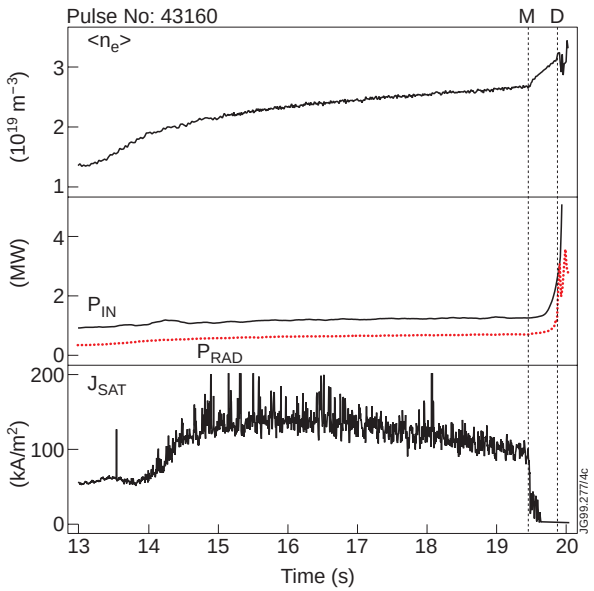

Figure 5: Time evolution of the volume averaged plasma density, the total input power, the radiated power and J_{sat} from a Langmuir probe close to the inner strike point for an Ohmic density limit shot in a vertical target configuration. The times marked are for the MARFE limit ('M') and the disruption limit ('D').

figure 3), an X-point MARFE forms (as monitored by the bolometry and by visible spectroscopy from the top of the machine). The fuelling efficiency is then suddenly increased and the rate of rise of the density increases. In this phase the plasma is strongly detached from the divertor and the J_{sat} decreases dramatically. Shortly after the formation of the X-point MARFE, at ~19.8 s, a thermal instability is reached in the main plasma and the radiation rises strongly (time 'D'), leading to a disruption.

In this section we report on D_α measurements obtained with KT6A in Ohmic and L-mode density limit discharges. Results from both Mark IIA and Mark IIAP divertor experiments have been studied but, up to now, no difference in the D_α emission has been observed between these two divertors.

4.1. Time evolution of D_α emission

We analyse the D_α emission from the ohmic density limit discharge of figure 5 (Pulse 43160). The magnetic equilibrium of this discharge is shown in figure 3, where it can be seen that channel 6 intersects the vertical target close to the strike point. The time evolution of the D_α intensity from tracks 4 to 10 is plotted in figure 6. Except for channel 6, which is near the watershed between private and SOL regions, the signal intensities for all the other tracks increase almost linearly with density. At t=19s, 400ms before the onset of the MARFE, the signals from channels 4, 5 and 6 drop dramatically, while the emission from channels 7 and 8 increases sharply, indicating a movement of the D_α emission peak further upstream in the inner SOL.

We define Rda as the ratio of the D_α signal from channel 7 to that from channel 6, $\mathrm{Rda} \equiv I_7(D_\alpha) / I_6(D_\alpha)$. Rda is plotted in figure 7 together with the degree of detachment,

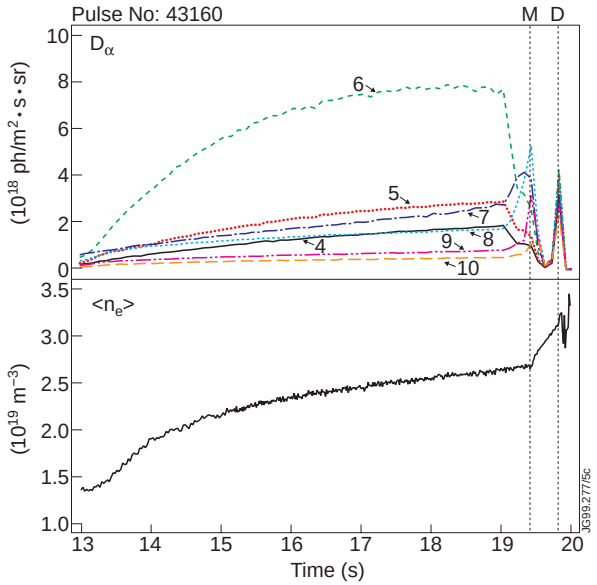

Figure 6: Time evolution of the D_α emission measured by KT6A along tracks 4 to 10 (see figure 3) and of the volume averaged plasma density for an Ohmic density limit shot with vertical target configuration.

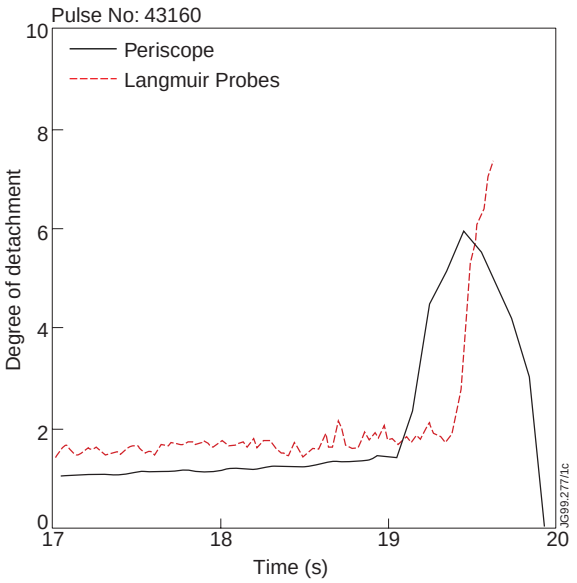

Figure 7: Time evolution of the the degree of divertor detachment, defined using the Langmuir probes [3] and using two adjacent channels of the divertor periscope, for an Ohmic density limit pulse.

$\mathrm{DoD} \propto n_e^2 / J_{sat}$, defined using the measured ion saturation current [3]. It is worth noting that in spite of the fact that these two calculations are totally independent, they both exhibit a similar time evolution. This is despite the fact that the Rda is based on integrated measurements over the channel length, while the Langmuir probes deliver local data. The DoD increases sharply about 250 ms after the sharp increase in Rda. Therefore, the Rda can be foreseen as a useful tool for the characterisation of the detachment, complementary to the DoD. Both DoD and Rda are potential candidates for being adapted into a feedback system for detachment control in real time during pulses.

In horizontal target discharges, one could redefine Rda as the D_α ratio between channels 4 and 5, $\mathrm{Rda} \equiv I_4(D_\alpha) / I_5(D_\alpha)$. While these ratios are not optimised for these measurements due to the poor time resolution of the diagnostic (100 ms), this could be improved significantly by using a photomultiplier-based detection system.

4.2. Spatial location of the D_α emission peak

Due to the strong dependence of the total magnetic field strength on major radius, R, it is possible to determine the spatial location, in terms of an emission-weighted average R, of the D_α emission from the Zeeman splitting of the spectrum. With the precision possible in our fitting procedure and since the divertor periscopes view approximately perpendicular to major radius, it is possible to localise this average position of emission to ± 2.5 cm. Knowledge of the location of the emission provides information on the energy distribution of the atoms, as will be shown in the next section.

Figure 8 shows the average major radius of the D_α emission as a function of plasma density for pulse 43160. For $n_e < 2.6 \times 10^{19}$ m^{-3}, the radius of emission from all channels in the main SOL remains constant and close to the vertical target plate (shown with the dashed line marked 'S' in figure 8), with the exception of channel 6. In the case of channel 6, which views the SOL close to the strike point, the radial location of D_α emission moves from the target up the inner leg as the density increases. This may be associated with detachment beginning at the strike point and only later spreading out into the SOL, something which has been predicted by modelling and confirmed in experiment for vertical target discharges [3].

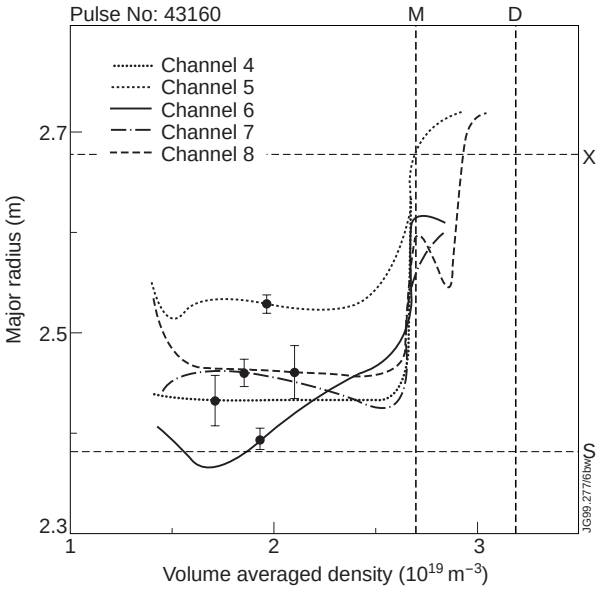

Figure 8: Location of the maxima of D_α emission for tracks 4 to 8 of the divertor periscope as a function of the volume averaged plasma density for an Ohmic density limit pulse. The densities corresponding to MARFE formation ('M') and the disruptive limit ('D') are shown as are the major radii of the strike point ('S') and the X-point ('X').

At low to moderate densities, channel 5, which views the private plasma region, exhibits a maximum of D_α emission located at about 2.52 m. It is not clear whether this is due to detachment of the private plasma from the divertor or to an averaging of emission from the inner private plasma and the outer main SOL. Interestingly, the average emission radius from channel 4 is ~2.42 m, consistent with emission from the corner of the divertor, something which has been observed in horizontal target discharges [6] but not, until now, in vertical target configurations.

Above a density of 2.6×10^{19} m^{-3} all the measured emission locations shift quickly to larger major radius. By the time of the X-point MARFE formation, the D_α emission is indeed measured to be near the X-point radius (the dashed line marked 'X' in figure 8). This is true of the channels viewing the private plasma as well as of those viewing the inner divertor main SOL.

Figure 9 shows a cross section of the inner divertor with the location of the maximum emission for $n_e = 1.6\times10^{19}$ m^{-3} (the beginning of the density ramp, attached plasma phase) and for 2.7×10^{19} m^{-3} (just before the onset of the X-point MARFE, detached plasma phase). While the plasma is attached, the emission in the main SOL seems to follow the 1 cm flux line (as referenced to the outer midplane). The movement of the region of maximum emission to the X-point at the time of the MARFE is also clear.

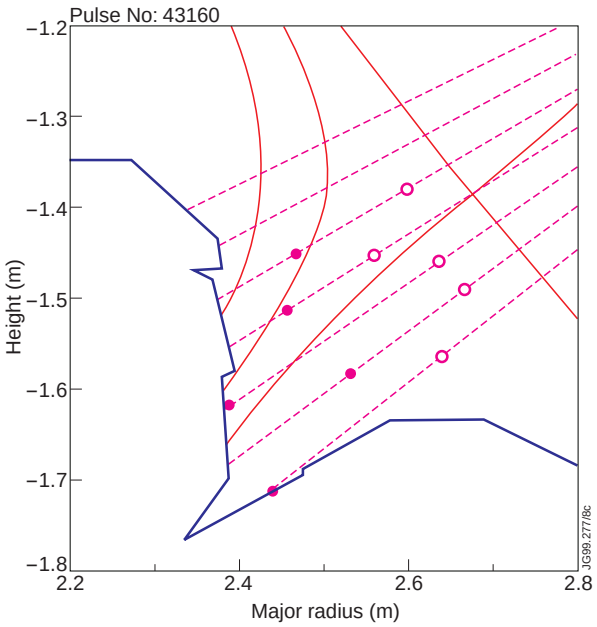

Figure 9: Cross section showing the location of the maximum D_α emission for pulse 43160 at the start of the density ramp (filled circles) and at the time of the X-point MARFE formation (open circles).

In addition to the Zeeman splitting measurements, it is possible to deduce the average major radius of D_α emission using a fast CCD camera which is mounted at the top of the machine and looks down vertically on the divertor. Since the line of sight of this camera is parallel to the inner vertical target plates, this CCD system is not strongly sensitive to shifts in emission in plasmas in vertical target geometries. In particular, local detachment of the emission at the separatrix is usually not observed as the line integral through the main SOL results in the emission maximum staying close to the target. For this reason, we prefer to compare the two measurements of the location of the D_α emission in a discharge limited on the horizontal divertor target plates.

The average position of D_α emission, as measured by several channels in KT6A, is shown in figure 10 for an Ohmic density limit discharge in a horizontal target configuration. Also shown

is the major radius of the pixel in the vertically viewing CCD camera which measures the highest signal. Up to the formation of the MARFE, this radius oscillates between the position of the inner divertor strike point ('S') and the position of the inner corner of the divertor, where a local maximum of the D_α emission has been observed previously [6]. At the time of the X-point MARFE formation, the emission from the strike point disappears and a peak in emission at the X-point appears. The intensity of this peak is initially smaller than the line integral of the emission from the divertor corner (which may be strongly weighted due to the long viewing length along the vertical target) and the maximum position as measured by the CCD camera only jumps to the X-point about 250 ms after the MARFE formation.

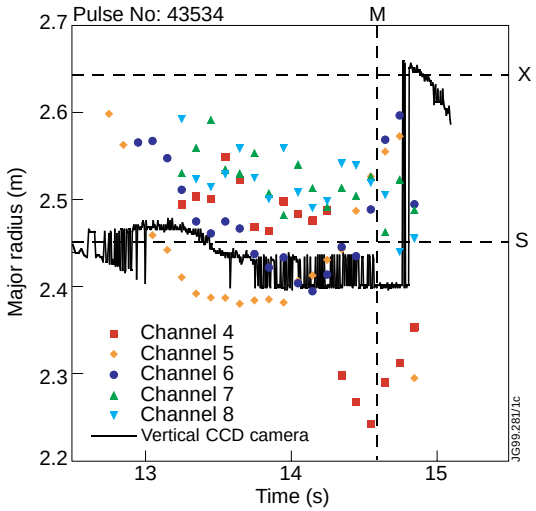

Figure 10: Time evolution of the position of the maximum emission of D_α deduced with Zeeman splitting, from KT6A, and measured with the CCD camera viewing from the top of the machine. Ohmic density limit shot (#43534) in a horizontal target configuration.

The position of maximum D_α emission as measured by KT6A is in fair agreement with the CCD camera. Channel 5 appears to favour the emission from the divertor corner rather than the strike point. This is consistent with this strike point emission being located very close to the horizontal target and thus out of the field of view of channel 5. As the view of KT6A moves further out into the main SOL (channels 6-8), the position of the maximum D_α emission gradually increases. In the attached phase of the discharge, the maximum emission in the main SOL thus again roughly follows the 1 cm magnetic flux contour. A significant increase in the radius of emission measured in channels 5 and 6 is seen before the X-point MARFE onset. Indeed, detachment in horizontal target configurations has been observed to begin in the divertor corner [6]. Such a shift is not observed in channels 7 and 8. Since these channels view above the X-point in horizontal configurations, they may well be not greatly affected by divertor detachment.

The greatest difficulty with the comparison given in figure 10 is the behaviour of channel 4 of KT6A. While the measured emission maximum begins near the strike point, this position jumps to unphysically low major radii at the time of the onset of detachment in the divertor corner. This behaviour is not understood.

4.3. Measurement of the neutral atom energies in density limit discharges

From the full width half maximum (FWHM) of the narrow (Franck Condon) and the broad (charge exchange and reflected) components of the D_α spectrum, it is possible to estimate the energy distribution of the deuterium neutrals. Assuming that the energy distribution of the atoms is Maxwellian, fitting the spectrum with a gaussion allows to write:

$$e^{-(\lambda-\lambda_0)^2/2\sigma^2} = e^{-mv^2/2kT}, \tag{5}$$

where λ is the wavelength of the spectrum, λ_o is the central wavelength,

$$\sigma = \frac{FWHM}{2\sqrt{2\ln(2)}}, \tag{6}$$

m is the mass of the ion, v the component of the ion velocity along the line of sight, k is the Boltzmann constant and T the temperature.

From (5) and (6), the energy of the atoms is derived:

$$T[eV] = 1.679 \times 10^8 \; m[amu]\left(\frac{FWHM}{\lambda_0}\right)^2. \tag{7}$$

The fitting uncertainties in the deduced energies are found to depend on the strength of the signal. For channels with good signal strength (near the strike point), the uncertainty in the energy of the cold component of the neutrals is 6%, dropping to 4% at higher density. The uncertainty in the width of the broad component is larger, dropping from 40% to 20% as the density is increased.

The energy of the slow atoms (derived from the narrow component fit) is shown as a function of the volume averaged plasma density in figure 11 for the vertical target Ohmic density limit pulse. The energy varies from channel to channel, suggesting that different emission mechanisms are important in different parts of the divertor plasma. The lowest neutral energy is measured in channels 5 and 6 which are the two views closest to the inner divertor strike point and correspond to the position where detachment begins. In all channels the average energy of the slow atoms decreases gradually as the density increases until, just before the X-point MARFE formation, the energy of emission in all channels drops to 1 eV. This is in contrast to recent results from JT-60U [4], where the width of the cold component is seen to increase with increasing density. There being no full collisional radiative model which includes deuterium atoms, molecules and molecular ions, it is difficult to know what is the cause of this difference.

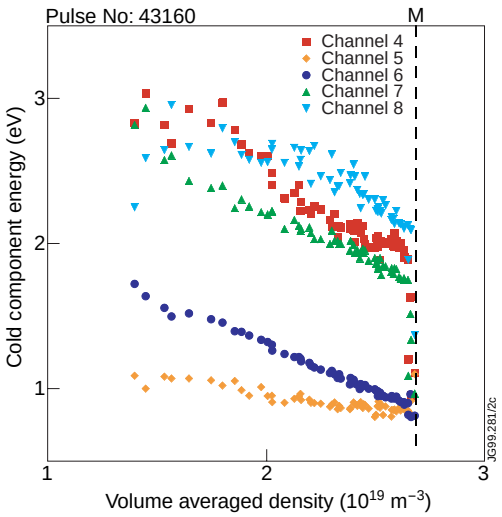

Figure 11: Deuterium atom energy derived from the narrow component of the D_α spectrum as a function of volume averaged core density for a vertical target, Ohmic density limit pulse.

The ion temperature deduced from the broad component (charge exchange + reflection) is shown in figure 12 as a function of the volume averaged plasma density for the same Ohmic density limit pulse. In the SOL (channels 7 and 8) as well as in the private region

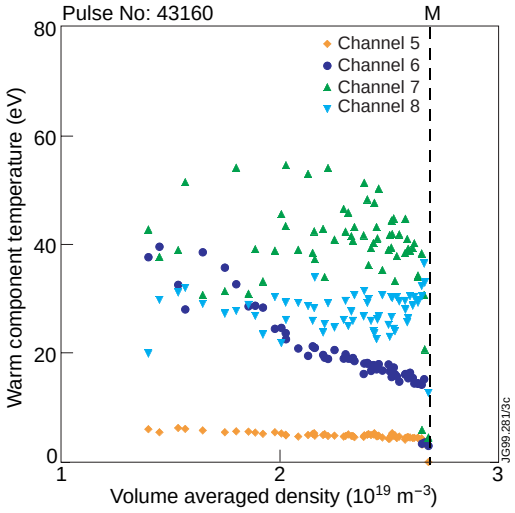

Figure 12: Ion temperature derived from the broad component of the D_α spectrum as a function of volume averaged core density for a vertical target, Ohmic density limit pulse.

(channel 5), there is nearly nochange in the deduced ion temperature as the density is increased. For channel 6, which views close to the inner strike point, the ion temperature decreases from about 40 eV at low density to 15 eV just before the MARFE formation. As with the average position of the emission (figure 8), the initial detachment appears to be localised close to the divertor strike point.

For comparison, an L-mode density limit shot (pulse 43161) in the same configuration as the Ohmic density limit shot has been analysed. In the L-mode pulse, the input power was increased from 1.4 to 2.8 MW using neutral beam injection. The density limit (at the MARFE) was found to increase from 2.7 to 3.3×10^{19} m^{-3}. The radiating power fraction during the density rise up to the MARFE remains close to 50%.

Figure 13 shows the emission-averaged radial position of the D_α emission as a function of the plasma density. As in the Ohmic pulse, the emission location moves from the vertical target to the X-point radius as the density is raised to the MARFE limit. In contrast to the Ohmic pulse where only the line of sight viewing the X-point exhibited any significant detachment at moderate densities, several of the viewing chords in both the private plasma and in the main SOL observe a gradual shift in the emission to larger radii as the density is increased. We thus conclude that detachment is somewhat less localised in L-mode pulses, perhaps due to the increased power flow down the SOL.

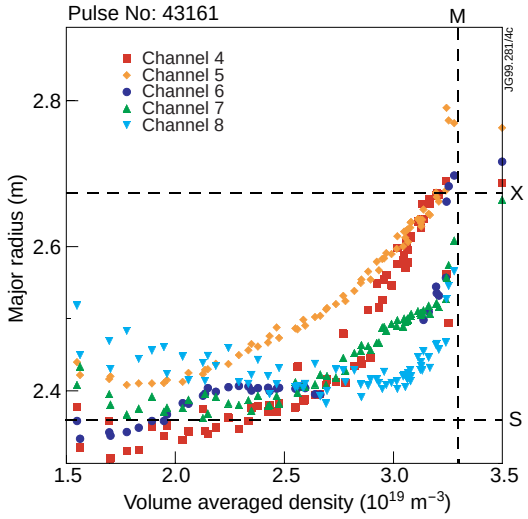

Figure 13: Location of the maxima of D_α emission for tracks 4 to 8 of the divertor periscope as a function of the volume averaged plasma density for an L-mode density limit pulse. The density corresponding to MARFE formation ('M') is shown as are the major radii of the strike point ('S') and the X-point ('X').

The atom and ion temperatures deduced from the narrow and broad components of the D_α spectra are shown for the L-mode pulse in figures 14 and 15. Both the trend and the absolute values of the energy of the cold atoms are very similar to those observed in the Ohmic discharge (figure 11). In contrast, it appears that the ion temperature in the SOL is actually lower in the L-mode pulse as compared to the Ohmic pulse (figure 12).

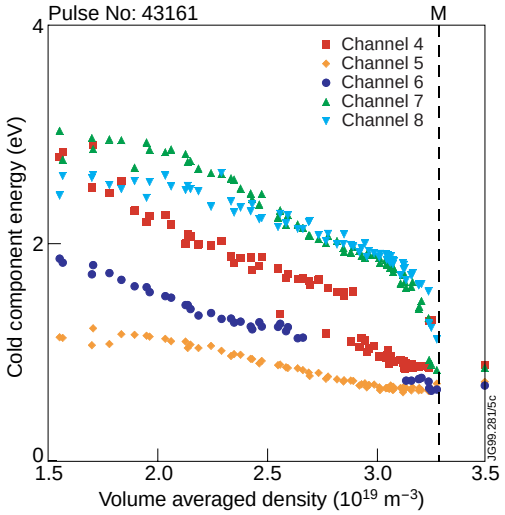

Figure 14: Deuterium atom energy derived from the narrow component of the D_α spectrum as a function of volume averaged core density for a vertical target, L-mode density limit pulse.

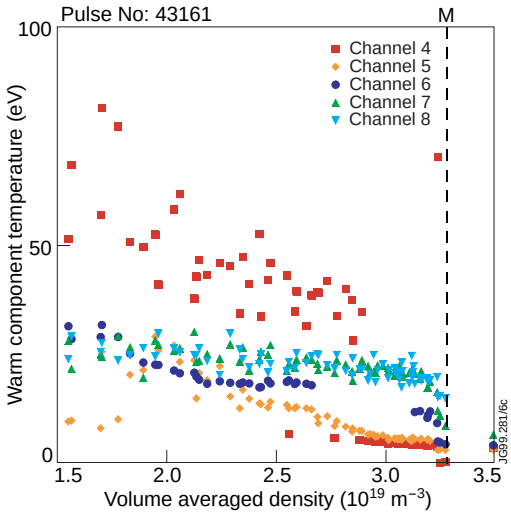

Figure 15: Ion temperature derived from the broad component of the D_α spectrum as a function of volume averaged core density for a vertical target, L-mode density limit pulse.

There is clearly a problem with the fit to the ion temperature of channel 4 at low densities. The fitting routine produces uncertainties which are larger than the deduced temperature for these fits and the values cannot thus be trusted. At higher densities (above 2.8×10^{19} m^{-3}), the fit converges to much lower temperatures (~5 eV), very similar to those found in the other channel which views the private plasma.

It is interesting to the compare the deduced ion temperatures to the electron temperatures measured by the target Langmuir probes. The electron temperatures and densities derived from several probes near the strike point of the Ohmic density limit pulse are shown in figure 16. The two probes closest to the strike point are probes 7 and 8 and they can be compared to channel 6 of KT6A. The most noticeable feature of the two measurements is that the ion temperature is significantly greater than the electron temperature at low to moderate densities. This is consistent with upstream ion temperature measurements made with a retarding field analyser [7,8] which also found $T_I > T_e$. Indeed, the decrease of ion temperature with increasing density may be due to increased ion-electron equipartition power as the density is raised. At the density just before the MARFE, both the electron and ion temperatures near the separatrix are measured to be 15 eV. The electron and ion temperatures in the private plasma

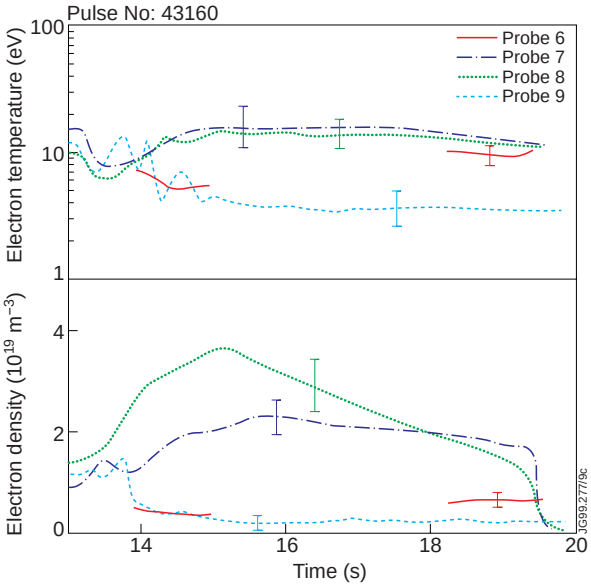

Figure 16: Time evolution of electron temperature and the electron density on the inner vertical target measured with Langmuir probes. The data are for an Ohmic density limit pulse.

are measured to be approximately equal at ~5 eV and do not vary significantly with density. Much larger ion than electron temperatures are deduced in the main SOL but this is to be expected since the D_α emission in these KT6A channels was found to be coming from a region significantly upstream of the targets (figure 9).

5. COMPARISON TO DIVERTOR MODELS

The measured D_α spectral shapes have been compared to the results of our divertor modelling codes. These preliminary comparisons are based on the results of existing modelling of Ohmic and L-mode density limit discharges [9].

The divertor modelling presented in this report was performed using the EDGE2D two dimensional fluid code [10] which incorporates the NIMBUS Monte Carlo neutral package [11]. The assumptions used in the simulations and their uncertanties are described in [9]. NIMBUS has been modified to calculate and output the first and second moments of the neutral velocity distribution for each cell in the computational grid. The moments are also available separately for neutrals following charge exchange events and for reflected and Franck-Condon neutrals before they have undergone any charge exchange reactions. These moments, which are available in all three dimensions, are used in a postprocessor code to calculate the D_α spectrum viewed along a particular line of sight. Currently, the postprocessor assumes that the viewing line is in the poloidal plane although extension to viewing lines with a toroidal component is possible. Emission following dissociative excitation of D_2 molecules is currently not included in the model. This has been shown to be important in JT-60U [4] and inclusion of this process in our model is being considered.

The simulated D_α spectrum for track 6 of KT6A is shown in figure 17. For this simulation, the geometry of the line of sight was approximated by a straight line in the poloidal plane. This is not thought to introduce significant errors into the calculation since KT6A views almost completely poloidally across the divertor (see figure 3). Other limitations include the lack of an instrument function in the simulation, no emission from neutrals during recombination and no account for the width of the viewing line. The lack of an instrument function will lead to a mismatch between

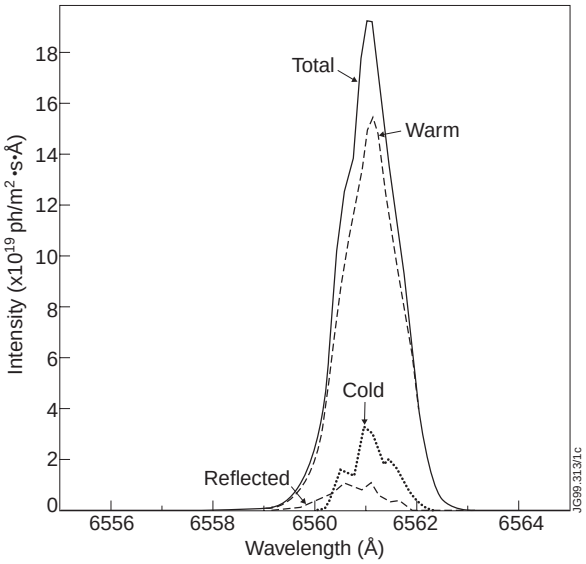

Figure 17: Simulated spectrum for D_α emission along track 6 of KT6A. The simulation is for an Ohmic density limit pulse with separatrix density of $1.5\times10^{19}\ m^{-3}$ and should be comparable to the measured spectrum in figure 2. The simulated spectrum is divided into contributions from cold (Franck-Condon) neutrals, from reflected atoms and from neutrals which have undergone at least one charge exchange reaction. Emission from neutrals during free electron recombination is not yet included in the spectrum.

simulation and measurement for very low temperatures (the instrument function is equivalent to 0.6 eV for D_α). The simulation on which the spectrum in figure 17 is based is for an Ohmic density limit pulse with a high separatrix plasma density plasma, $n_{sep} = 1.5 \times 10^{19}\ m^{-3}$, which is thought to correspond to a volume averaged density of about $< n >= 2.5 \times 10^{19}\ m^{-3}$, i.e. near the MARFE density limit.

The simulated spectrum in figure 17 can be compared to the measured spectrum shown in figure 2. The most noticeable difference between the two spectra is the relative intensity of the warm to cold components. The warm components in the spectrum are very small, too small to be shown in figure 2. The simulation, on the other hand, predicts a warm charge exchange component which dominates the spectrum. One of the conclusions found in [4] and [9] was that there was a serious discrepancy between the model and experiment for deuterium emission. The comparison between figures 2 and 17 shows that this discrepancy applies also to deuterium line shapes. This is an area where further work is needed. It is hoped that the measurements presented here will help to identify and resolve the problems in the neutral transport model.

6. CONCLUSIONS AND PERSPECTIVES

The spectral shape of the D_α emission from the JET divertor has been investigated using the KT6A divertor periscope. Useful information has been obtained on neutral density and energy distributions. The results are shown to be sensitive to the alignment of the periscope in the machine. An in situ technique for measuring this alignment, using pulses originally designed for calibrating the divertor Langmuir probes, has been demonstrated. The periscope alignment is found to be slightly shifted relative to its design value but to be stable over a long period of plasma operation.

The ratio of the D_α intensities from adjacent viewing channels of KT6A has been shown to be a sensitive monitor of divertor detachment. Simple modifications of the detection instrumentation which could make this monitor available in real time to the plasma operator have been proposed.

The average position of the D_α emission along the KT6A lines of sight has been deduced from the Zeeman splitting. This provides unique information of the spatial distribution of neutrals in the divertor. The neutrals are seen to progressively move from the target towards the X-point as the plasma density increases and the divertor plasma detaches.

The energy distribution of the neutrals in the divertor has also been studied. The neutrals naturally divide into ‘cold’ and ‘warm’ components corresponding to Franck-Condon neutrals and reflected or charge exchanged neutrals, respectively. The average energy of the cold neutrals is seen to change as the density is increased, suggesting that the main production path of these neutrals is changing with the divertor conditions. This is similar to results reported by JT-60U [4]. The energy of the warm component also changes as the plasma density is increased and may

provide information on the ion temperature in the divertor. Detailed modelling to separate reflected and charge exchanged neutrals is required to confirm this hypothesis.

The fitting routine used in this study is an old version of a code which was designed for separating hydrogen isotopes in the D_α spectrum rather than for detailed study of the shape of the warm component. This has meant placing non-physical restrictions on the fit parameters (see Appendix A). Future work will include generalising the routines so that only physically meaningful constraints are applied to the fit.

Measured neutral density and energy profiles place a severe constraint on divertor modelling. A first comparison between measurement and model shows significant discrepancies. In particular, the model appears to greatly overestimate the emission from warm neutrals which have experienced at least one charge exchange reaction. Improving the neutral transport models in our codes is clearly necessary. Consideration is being given to better molecular modelling and to the influence of non-Maxwellian electron distribution functions in the divertor plasma.

REFERENCES

[1] P.D. Morgan and C.H. Wilson, "Visible Spectroscopy of the JET Pumped Divertor using Coherent Optical-Fiber Bundles", Rev. Sci. Instrum. **66** (1995) 606-608.

[2] H. Kubo, private communication.

[3] A. Loarte, R.D. Monk, J.R. Martín-Solís et al., "Plasma Detachment in JET Mark I Divertor Experiments", Nucl. Fusion **38** (1998) 331-371.

[4] H. Kubo, H. Takenaga, T. Sugie et al., Plasma Phys. Control. Fusion **40** (1998) 1115-1126.

[5] A.C. Maas, P. Andrew, P. Coad et al., "Diagnostic Experience during Deuterium-Tritium Experiments in JET, Techniques and Measurements", Fusion Technology 1998, vol.1, (Proc. 20th Symposium on Fusion Technology, Marseille, France, 7-11 September 1998) 693-696.

[6] C.F. Maggi, L.D. Horton, G. Corrigan et al., "Modelling of Deuterium Emission in High Density Divertor Plasmas in JET", J. Nucl. Mater. **266-269** (1999) 867.

[7] H.Y. Guo, G.F. Matthews, S.J. Davies et al., "Ion Temperature Measurements in JET Boundary Plasmas using a Retarding Field Analyser", Contrib. Plasma Phys. **36** (1996) 81.

[8] S.K. Erents, P. Breger, S.J. Davies et al., "Assessment of the DIVIMP 'Onion-Skin' Model in the JET Mark I Divertor", J. Nucl. Mater. **241-243** (1997) 433.

[9] C.F. Maggi, R.D. Monk, L.D. Horton et al., "The Isotope Effect on the L-mode Density Limit in JET H, D and T Divertor Plasmas", to appear in Nucl. Fusion.

[10] R. Simonini et al., Contrib. Plasma Phys. **34** (1994) 368.

[11] E. Cupini, A. DeMatteis and R. Simonini, NET Report EUR XII-324/9, CEC (1984).

APPENDIX A: TECHNICAL DETAILS OF THE SPECTRUM FITTING

A least squares multi-gaussion fitting program was used to fit the spectrometer data. The load module, JETSTP.KS3B.LOAD(FITZEM), was run from the CLIST JETLOA.LIB.CLIST(FITZEM).

The two main data input files were JETLOA.KS3B.DATA(SETUP94) and (ESTIMAT). SETUP94 informed the program which spectra from which CCD camera were to be fitted, and whether the program should generate a public or private PPF (or neither). ESTIMAT defined the number of gaussions to be fitted, and provided the first estimates of all the parameters (intensity, line-centre position, line-width) for the minimisation routines and defined any linking between parameters (i.e. forcing common linewidths or relative intensities or positions). In order for the least-squares minimisation in FITZEM to converge quickly, the number of free parameters should be reduced, where possible, by linking them to others. Any parameter, P(x), could be linked to any other by the formula

$$P(x) = P(y)*FACTOR + OFFSET. \qquad (A.1)$$

The ESTIMAT file also defined the pixel range to be used by the fitting program, and the switches that turned on the Zeeman splitting (and isotope shift, if H and D are fitted) features.

FITZEM is a development (by M. Stamp) of the original FITNG (due to W. Mandl). It was designed to fit Zeeman-split spectra from a mixture of hydrogen and deuterium. Due to restrictions on the number of gaussions in the code, only one 'warm' component, but a full three 'cold' components are fitted, for each species. Hence the first 3 gaussions (as defined in ESTIMAT) are assumed to be the Zeeman split 'cold' deuterium components, while the 4^{th} is the 'warm' deuterium component. Similarly, gaussians 5 to 7 are the Zeeman split 'cold' hydrogen components, whilst the 8^{th} is the 'warm' hydrogen component. FITZEM assumes that the first gaussian (defined in ESTIMAT) is the π-component of deuterium, and gaussians 2 and 3 the σ^- and σ^+ components, whilst gaussians 5,6,7 are the hydrogen π, σ^- and σ^+ components, respectively.

The minimisation routines in FITZEM utilise Eq. A.1 to maintain the linking of parameters during the least squares fitting. If the ZSPLIT parameter (representing the deuterium Zeeman splitting, in pixels) in the ESTIMAT data file is non-zero, then the Zeeman splitting pattern is imposed on the hydrogen and deuterium π, σ^- and σ^+ components by the formula

$$P(x) = P(y) + (Z1)*ZSPLIT + ISOTOPE\_SHIFT \qquad (A.2)$$

where P(y) is the line position of the cold deuterium π component and Z1 and ISOTOPE_SHIFT are defined according to:

	Z1	ISOTOPE_SHIFT
deuterium σ^- cold component	-1	0
deuterium σ^+ cold component	+1	0
hydrogen σ^- cold component	-1	+16.5 (for KS3B)
hydrogen σ^+ cold component	+1	+16.5 (for KS3B)

If ZSPLIT=0 in ESTIMAT, Eq. A.2 is still used but ZSPLIT is calculated from the magnetic field PPF, MAGN/BVAC, for the first spectrum to be fitted. For subsequent spectra ZSPLIT is calculated from the fitted π to σ^- splitting from the previous spectrum (i.e. difference in positions of gaussians 1 and 2).

Note that if ISOTOPE_SHIFT = 0 in the ESTIMAT input file, then Eq. A.2 is NOT applied.

The KS3B PPF generated by FITZEM produces many nodes, with the assumption that D and H spectra are being fitted (3 cold + 1 warm of each). However, the flexibility of the data input files (namely ESTIMAT), means that the code can easily be run for 3 cold and 3 warm deuterium components, and no hydrogen. In this case, some of the PPF nodes, such as KS3B/HTHD, the H to H+D ratio, will be nonsense.

Appendix B lists the ESTIMAT file used for the data in this report. Hydrogen fractions were very low in #43160 and #43161, so hydrogen is not fitted (ISOTOPE_SHIFT = 0), and there are 6 gaussians defined: 3 cold and 3 warm deuterium components.

The intensity, position and width of the first gaussian (π-component of D) are all free parameters in the fits. Gaussions 2 and 3 are forced to have the same FWHM as gaussian 1 (i.e. they all have the same 'cold' temperature). The position of gaussian 3 is offset from gaussian 1 by a fixed 5.9 pixels (an average π to σ^+ Zeeman splitting), though the position of gaussian 2 is a free parameter (remember that the splitting between gaussians 1 and 2 is interpreted by FITZEM as ZSPLIT, so the PPF node KS3B/ZEEM [the magnetic field deduced from ZSPLIT] is still meaningful). Note that gaussians 2 and 3 are not forced to have equal intensities (or half the intensity of gaussian 1), so these intensity ratios can be used to check the 'goodness' of the fits. Gaussian 4 is the warm π-component. Its intensity and width are free parameters, but its position is fixed exactly (NB no offset) to gaussian 1. Gaussians 5 and 6 are defined totally in terms of the others. Their intensities are set to half that of gaussian 4, and the widths set equal to that of gaussian 4. Their positions are set equal to that of gaussian 1 (=4), with fixed offsets of $\pm$5.9 pixels (i.e. they are assumed to have a FIXED Zeeman pattern).

A fitted KT6 spectrum (#43160, track 6, frame 97, t=57.95s) is shown in fig. 2, where the individual π, σ components are plotted at half intensity. Note the goodness of the fit, and the low relative intensity of the warm components.

KS3B spectra taken with a suitably orientated linear polariser show just the π-component. These spectra are clearly asymmetric, with a tail on the short wavelength side. They can still be reasonably well fitted (with similar program FITHDT) with two gaussians provided that the warm component can have a different central wavelength from the cold component (fig. 1, #43160, track 4, frame 151, t=54.67s). Note that the fit is worse in the line-wings, and the higher relative intensity of the warm component. This KS3B spectrum was from a near-vertical view close to the inner strike point.

Any further work in this field should be preceded by modifications to the FITZEM code. An option for single isotope fitting should be included, and implemented to expect 3 cold and 3 warm gaussian components. There should be proper treatment of the Zeeman splitting (Eq. A.2), and the ESTIMAT file should be modified to allow a wavelength shift between the cold and warm components.

APPENDIX B: INPUT FILE USED FOR SPECTRUM FITTING: JETLOA.KS3B.DATA(ESTIMAT)

```
ESTIMATES 2.8T PROGRAM FITNG >>>>> D-ALPHA <<<<< AND H-ALPHA(395)

6570
5.0                  <— BACKGROUND P(1)
6                    <— NUMBER OF GAUSSIANS
1     9.00000E+03    352.000   4.000    1   1   1       P(2,3,4)
2     4.50000E+03    345.000   4.000    1   1   0       P(5,6,7)
3     4.50000E+03    358.000   4.000    1   0   0       P(8,9,10)
4     3.00000E+03    352.300   25.000   1   0   1       P(11,12,13)
5     3.00000E+03    352.300   25.000   0   0   0
6     3.00000E+03    352.300   25.000   0   0   0

1     0.0            0.000     0.000    0   0   0       OFFSET()
2     0.0            -5.900    0.000    0   3   4
3     0.0            +5.900    0.000    0   3   4
4     0.0            0.000     0.000    0   3   0       OFFSET()
5     0.0            -5.900    0.000    11  3   13
6     0.0            +5.900    0.000    11  3   13

1     1.100          1.000     1.000                    FACTORS()
2     1.000          1.000     1.000
3     1.000          1.000     1.000
4     1.000          1.000     1.000
5     0.500          1.000     1.000
6     0.500          1.000     1.000

0.0   0.0            ZSPLIT, ISOTOPE SHIFT : (AUTO ZSPLIT, IF ZSPLIT=0)

1
330   390            (Pixel range included in the fitting)
```